Direct Observation of Large Altermagnetic Splitting in CrSb (100) Thin Film

Sen Liao[1,2], Xianglin Li[1,2], Xiuhua Chen[1,2], Ziyan Yu[1,2], Jianghao Yao[1,2], Rui Xu[1,2], Jiexiong Sun[1,2], Zhengtai Liu[4], Dawei Shen[3], Yilin Wang[1,2], Donglai Feng[2], and Juan Jiang[1,2*]

[1]*School of Emerging Technology, University of Science and Technology of China, Hefei 230026, China*
[2]*Hefei National Laboratory, Hefei 230088, China*
[3]*National Synchrotron Radiation Laboratory and School of Nuclear Science and Technology, University of Science and Technology of China, Hefei 230026, China*
[4]*Shanghai Synchrotron Radiation Facility, Shanghai Advanced Research Institute, Chinese Academy of Sciences, Shanghai 201210, China*

(Received 7 March 2025; accepted manuscript online 30 April 2025)

Altermagnets represent a newly discovered class of magnetically ordered materials. Among all the candidates, CrSb stands out due to its largest spin splitting energy and highest Néel temperature exceeding 700 K, making it promising for room-temperature spintronic applications. Here we have successfully grown high quality CrSb (100) thin film on GaAs (110) substrate by molecular beam epitaxy. Using angle-resolved photoemission spectroscopy, we successfully obtained the three-dimensional electronic structure of the thin film. Moreover, we observed the emergence of the altermagnetic splitting bands corresponding to the calculated results along the low symmetry paths $\bar{T}$–$\bar{Q}$ and $\bar{P}$–$\bar{D}$. The bands near the Fermi level are only spin splitting bands along the $\bar{P}$–$\bar{D}$ direction, with splitting energy reaching as high as 910 meV. This finding provides insights into the magnetic properties of CrSb thin films and paves the way for further studies on their electronic structure and potential applications in spintronics.

DOI: 10.1088/0256-307X/42/6/067503 CSTR: 32039.14.0256-307X.42.6.067503

Unlike conventional ferromagnets or antiferromagnets, a recently discovered class of magnetically ordered materials known as altermagnets has emerged. In a manner akin to antiferromagnets, altermagnets are characterized by compensated collinear order, with ferromagnetic spin alignment within each sublattice and an antiparallel inter-sublattice spin arrangement.[1–3] This symmetry enables alternating spin-splitting along the momentum direction, but with no net magnetic moment, resulting in distinct spin degeneracy at high-symmetry planes and spin splitting in the low-symmetry planes. This spin-splitting phenomenon, which does not rely on spin–orbit coupling (SOC), has generated significant interest for its potential applications in spintronics. Moreover, altermagnets combine the advantages of both ferromagnets and antiferromagnets, such as the ultrafast dynamics and resistance to external magnetic fields typical of antiferromagnets, along with the substantial spin-polarized currents and band splitting commonly seen in ferromagnets. As a result, altermagnets offer exciting opportunities for generating long-lived spin-polarized currents,[4–11] potentially giving rise to new transport phenomena, including spin torque[11–14] and the anomalous Hall effect.[15–21]

Based on the symmetry distribution of the spin in the reciprocal space, the altermagnetism can be further classified into g-, d-, and p-wave altermagnetism.[1,2,22] Several promising candidates have been identified through calculations, and most of them have also been experimentally verified. For instance, g-wave altermagnetism has been confirmed in MnTe,[23–27] where a 150 meV valence band splitting was observed parallel to the Γ–K direction in the alternating magnetic phase, which decreases toward the Néel temperature and vanishes in the paramagnetic phase.[26] Away from the high-symmetry points, the splitting energy can reach up to 0.8 eV.[27] The layered materials KV_2Se_2O and RbV_2Te_2O have demonstrated room-temperature metallic d-wave altermagnetism and C-paired spin-valley locking, presenting new avenues for spintronic applications.[8–11,28,29] Although RuO_2 has consistently been the most highly regarded candidate material for altermagnetism and has also exhibited anomalous Hall effects in transport measurements,[16] comprehensive spin angle-resolved photoemission spectroscopy (ARPES) measurements indicate that it does not exhibit alternating spin splitting in momentum space.[30]

Among these candidates, CrSb is particularly noteworthy due to its large spin splitting and a Néel temperature (T_N) exceeding 700 K,[2] making it highly suitable for room-temperature spintronic applications.[31] Due to the strong Kramers degeneracy, the spin splitting only exists outside the high-symmetry positions in the three-dimensional (3D) momentum space. Soft X-ray ARPES has been performed on the CrSb (100) thin films synthesized with magnetron sputtering, directly reveal-

*Corresponding author. Email: jjiangcindy@ustc.edu.cn
© 2025 Chinese Physical Society and IOP Publishing Ltd. All rights, including for text and data mining, AI training, and similar technologies, are reserved.

ing an altermagnetic band splitting of ∼0.6 eV.[32] Recent ARPES studies on CrSb (001) and (100) surfaces of cleaved single crystals confirmed a g-wave symmetry of its altermagnetism,[33–37] with the largest spin splitting observed on the (100) cleavage plane, reaching up to 0.93 eV.[33] Since the (100) plane is crucial to visualize the altermagnetism in CrSb, growing high-quality CrSb (100) thin films would benefit its future device fabrications based on the altermagnetism. Despite the previous soft X-ray ARPES work on CrSb (100) thin films, the high-resolution low-energy observation of band structure, especially near the Fermi level, is still needed to construct the details to understand the altermagnetism in CrSb (100) thin films.

In this study, we utilize high-resolution ARPES in combination with density functional theory (DFT) calculations to provide prototypical evidence for the 3D electronic structure and altermagnetic features in CrSb (100) thin films grown by molecular beam epitaxy (MBE). Our spectroscopic measurements are in overall agreement with the DFT calculations. Notably, we observe Kramers degeneracy at the high-symmetry directions in the momentum space, and prototypical signatures of altermagnetism-induced band splitting are observed away from these directions. Additionally, our photoemission spectroscopy results reveal a band splitting along the low-symmetry path $\bar{P}$–$\bar{D}$ in the 3D Brillouin zone (BZ) of up to 0.91 eV in agreement with the computational results, making it the largest splitting observed so far among all confirmed altermagnetic materials. The spin splitting bands near the Fermi level along the $\bar{P}$–$\bar{D}$ direction not only position CrSb (100) as a promising candidate for exploring the novel properties of altermagnetic materials but also underscore its potential for applications in spintronics.

Figure 1(a) shows the crystal structure of CrSb, which crystallizes in the NiAs-type structure ($P6_3/mmc$). The Cr atoms exhibit A-type collinear antiferromagnetic alignment of magnetic moments along the c-axis. The projection of the (100) plane is shown in the right panel of Fig. 1(a). The spin sublattices are connected through non-relativistic spin-group operations, denoted as $[C_2 \parallel M_z]$, where M_z represents the mirror symmetry operation, lifting the Kramers degeneracy. High-quality CrSb (100) thin film is grown on a GaAs (110) substrate by MBE. The low-energy electron diffraction (LEED) patterns of both the substrate and the thin film are shown in Figs. 1(b) and 1(c), respectively. Through the sputtering procedure, we achieved a clean surface of GaAs (110) with sharp LEED spots. The ratio of the two axes (a_2^* and c_2^*) of the thin film is close to 1.35, which is slightly different from the substrate (∼1.38), but closely matches the bulk CrSb, suggesting that there is almost no strain in our thin film and that the growth surface corresponds to the (100) plane of CrSb. Compared to the GaAs (110) pattern, the thin film exhibits a point with double the periodicity along the c-axis direction, indicating a 1×2 surface reconstruction in our thin film. The surface morphology, obtained by atomic force microscopy (AFM), is shown in Figs. 1(d) and 1(e). The thin film exhibits an island-growth mode with small

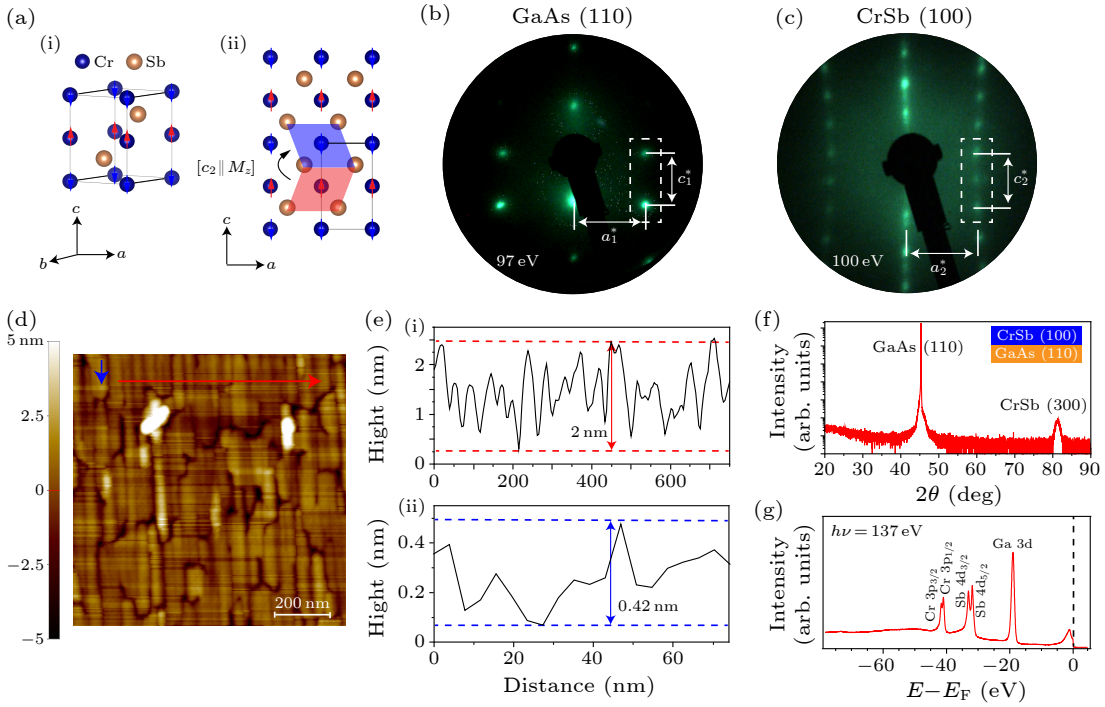

Fig. 1. Characterization of CrSb (100) Thin Film. (a)(i) 3D crystal structure of CrSb; (ii) Side view of the (100) plane. (b) LEED pattern of GaAs (110) substrate at an electron energy of 97 eV. (c) LEED pattern of CrSb (100) thin film at an electron energy 100 eV. (d) AFM image of the CrSb (100) thin film. (e)(i) The large-scale modulation of the thin film indicated by the red arrow in (d); (ii) the modulation within the island in the direction indicated by the blue arrow in (d). (f) XRD pattern of the CrSb (100) thin film, the inset shows a schematic of the interface. (g) Core-level spectra of CrSb, measured at a photon energy of 137 eV.

modulations of less than 2 nm over a large area and approximately 0.42 nm inside a single island, as shown in Fig. 1(e), indicating that each island is highly uniform. X-ray diffraction (XRD) measurements find a clearly separated film peak away from the substrate peak [Fig. 1(f)], which corresponds to the CrSb (300) peak. The absence of (100) and (200) peaks is due to the extinction rule in the hexagonal crystal system.[38,39] Therefore, our XRD result further confirms that the thin film is completely oriented along the (100) direction without any polycrystalline phases. Based on the (300) peak position, we can determine that the b^* axis of our film is ∼4.1 Å. Figure 1(g) shows the core level X-ray photoelectron spectroscopy data of the thin film obtained with 137 eV photons, where clear Cr $3p_{1/2}/3p_{3/2}$ and Sb $4d_{3/2}/4d_{5/2}$ peaks are observed, further indicating the correct phase of our thin film. Thus, combining various *in situ* and *ex situ* thin film characterizations, we confirm that our thin film is CrSb (100).

To obtain the 3D electronic structure of the CrSb (100) thin film, we perform photon energy-dependent ARPES measurements. Figure 2(a) presents the 3D BZ of CrSb with all the high-symmetry points indicated. Since the thin film is grown along the (100) plane, the directly measured plane at a certain photon energy in the reciprocal space corresponds to the plane perpendicular to the k_y direction, as indicated in green in Fig. 2(a). By scanning along the high-symmetry direction parallel to Γ–K by varying the photon energies, we can obtain the high-symmetry plane M–Γ–K, indicated in yellow in Fig. 2(a). Figure 2(b) shows the Fermi surface on the M–Γ–K plane, which is mapped with photon energies ranging from 90 eV to 150 eV. The Fermi surface exhibits C_6 symmetry, consistent with the calculated Fermi surface overlaid on the experimental results in Fig. 2(b). This symmetry allows us to determine the k_y-photon energy correspondence. With an inner potential estimated to be 6 eV, we find that 106 eV exactly cuts through the Γ–K direction, while 122 eV and 90 eV cut through the $\bar{\Gamma}_1$–$\bar{K}_1$ ($k_y = 0.4\pi$) and $\bar{\Gamma}_2$–$\bar{K}_2$ ($k_y = -0.4\pi$) directions, respectively, as indicated in Fig. 2(a). The constant energy contour at E_F-300 meV in the $\bar{\Gamma}_1$–$\bar{K}_1$–$\bar{A}_1$ plane is shown in Fig. 2(c), presenting a C_2 symmetry, consistent with the calculation. The high-symmetry cuts along the $\bar{K}_1$–$\bar{\Gamma}_1$–$\bar{K}_1$, $\bar{K}_2$–$\bar{\Gamma}_2$–$\bar{K}_2$, M_1–Γ, and Γ–M_2 directions are shown in Figs. 2(d)–2(g), respectively. All these band dispersions match well with the calculation, indicating that our k_y-photon energy correspondence is reasonable. Since the altermagnetism shows a strong Kramers degeneracy in CrSb, the corresponding high-symmetry cuts show no spin splitting as expected.

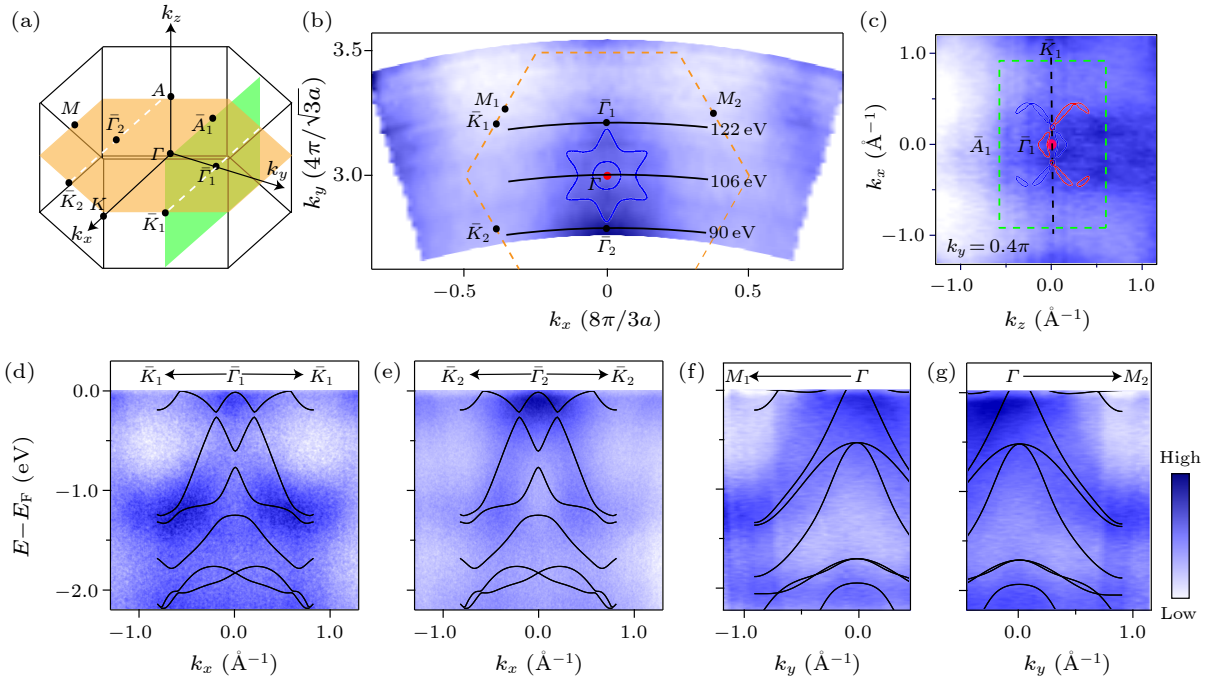

Fig. 2. Photon energy-dependent ARPES measurements with calculation fitting. (a) Schematic of the 3D BZ. The yellow hexagon plane outlines the K–Γ–M plane; the green rectangle plane outlines the $\bar{K}_1$–$\bar{\Gamma}_1$–$\bar{A}_1$ plane, which is parallel to the K–Γ–A plane. (b) Fermi surface on the K–Γ–M plane, with an integration energy range of ±50 meV; the black lines show the photon energy correspondence in the k_x–k_y plane. The Fermi surface indicated by blue lines is the calculated result. (c) Constant energy contour at $E_B = 300$ meV on the $\bar{K}_1$–$\bar{\Gamma}_1$–$\bar{A}_1$ plane ($h\nu = 122$ eV, $k_y = 0.4\pi$), with an energy integration range of ±200 meV. The black dashed line represents the $\bar{\Gamma}_1$–$\bar{K}_1$ direction. The calculated results are overlaid with blue and red, representing different spin directions. (d)–(g) Photoemission intensity plot along the $\bar{\Gamma}_1$–$\bar{K}_1$ direction ($h\nu = 122$ eV), the $\bar{\Gamma}_2$–$\bar{K}_2$ direction ($h\nu = 90$ eV), the M_1–Γ direction, and the Γ–M_2 direction, respectively; the spectra are normalized along the energy direction by a polynomial distribution extracted from $(k_x, k_y) = (0.95\,\text{Å}^{-1}, 1.05\,\text{Å}^{-1})$ to enhance the visibility of the states near the Fermi level. The calculated electronic structure is indicated by the black lines along with the experimental results. All data are taken at 8 K. All DFT calculations were performed without SOC.

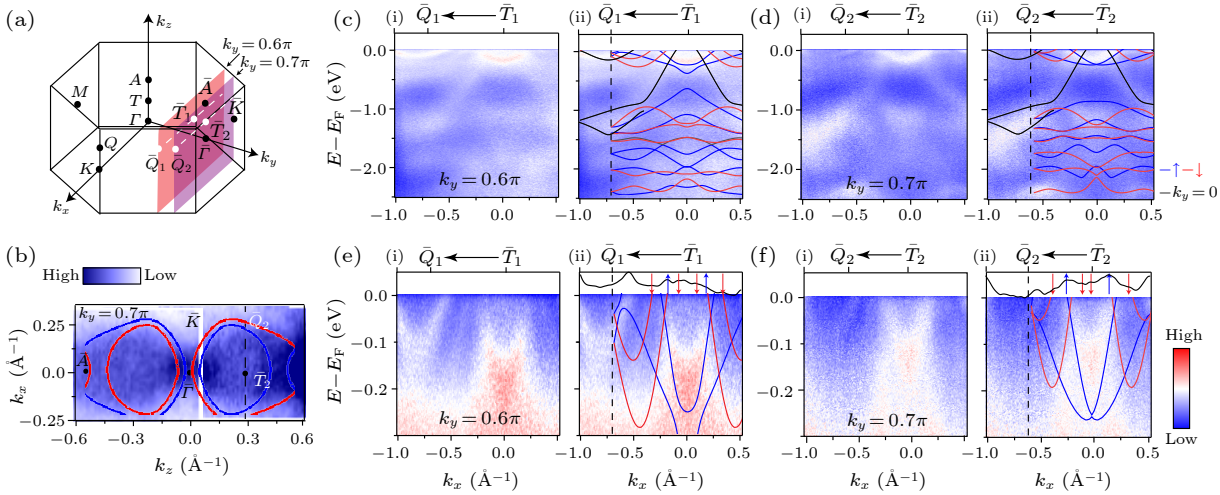

Fig. 3. Altermagnetic splitting along the $\bar{T}$–$\bar{Q}$ direction. (a) Schematic of the 3D BZ with highlighted measured low-symmetry planes. The red and purple rectangle planes refer to the low-symmetry planes at $k_y = 0.6\pi$ and $k_y = 0.7\pi$ away from the high-symmetry plane K–Γ–A, respectively. (b) Constant energy contour of the $\bar{K}$–$\bar{\Gamma}$–$\bar{A}$ plane at $E_B = 30$ meV, with an integration energy range of ± 20 meV ($k_y = 0.7\pi$, $h\nu = 21.2$ eV). (c)(i) Large range photoemission intensity plot along the $\bar{T}_1$–$\bar{Q}_1$ direction at $k_y = 0.6\pi$; (ii) same as (i) with appended calculation result. (d)(i) Large range photoemission intensity plot along the $\bar{T}_2$–$\bar{Q}_2$ direction at $k_y = 0.7\pi$; (ii) same as (i) with appended calculation result. (e) Zoomed-in spectra of (c) along the $\bar{T}_1$–$\bar{Q}_1$ direction at $k_y = 0.6\pi$. (f) Zoomed-in spectra of (d) along the $\bar{T}_2$–$\bar{Q}_2$ direction at $k_y = 0.7\pi$. The corresponding MDCs at the Fermi energy are plotted insets (e)(ii) and (f)(ii), with opposite spin splitting represented by red and blue arrows. The spectra of (c) and (d) are normalized along the energy direction by a polynomial distribution extracted from $k_x = 0.45$ Å^{-1} and 0.5 Å^{-1}, respectively, to enhance the visibility of the states near the Fermi level. All the data are taken at 13 K. All DFT calculations were performed without SOC.

To further verify the altermagnetism of the CrSb (100) thin film, we attempted to search for the predicted altermagnetic splitting along the low-symmetry directions in the 3D BZ. Figure 3(a) shows the positions of the two low-symmetry planes in the 3D BZ at $k_y = 0.6\pi$ and $k_y = 0.7\pi$, respectively. The constant energy contour along the $\bar{\Gamma}$–$\bar{K}$–$\bar{A}$ plane measured with 21.2 eV photon ($k_y = 0.7\pi$) at $E_B = 30$ meV is shown in Fig. 3(b). As predicted by the calculation, it exhibits two spin-antiparallel electron and hole pockets, which are located on either side of the $\bar{\Gamma}$ point. According to the calculation, the energy bands are spin-degenerate along the $\bar{\Gamma}$–$\bar{K}$ direction, whereas the spin is non-degenerate along low-symmetry directions such as $\bar{T}_2$–$\bar{Q}_2$ at $k_z = 0.5\pi$. The band dispersions along the $\bar{T}$–$\bar{Q}$ direction with $k_z = 0.5\pi$, measured in the $k_y = 0.6\pi$ and $k_y = 0.7\pi$ planes are presented in Figs. 3(c)(i) and 3(d)(i), respectively. The corresponding calculated band structure is overlaid on the experimental results [Figs. 3(c)(ii) and 3(d)(ii)]. The main electronic structure feature is composed of hole and electron bands with opposite spins near the Fermi level, along with flat bands at binding energies of around 1 eV and 2 eV. The overall calculation matches well with our experimental results except for the dispersive bands in the binding energy range of 0–1 eV. We find that it corresponds well with the calculated band at $k_y = 0$ along the T–Q direction, as indicated by the black lines. Therefore, we attribute this discrepancy to the k_y-broadening effect.[40] Figures 3(e) and 3(f) show the altermagnetic splitting near the Fermi level in these two directions, which are zoomed in from Figs. 3(c) and 3(d). The two hole-like bands and one electron-like band observed in the ARPES spectra correspond very well with the calculations. In both directions, the electron-like and hole-like bands have opposite spins, as indicated by the inset momentum distribution curves (MDCs) at k_F in Figs. 3(e)(ii) and 3(f)(ii), respectively. Thus, the splitting of multiple energy bands near the Fermi level along the two low-symmetry directions $\bar{T}$–$\bar{Q}$ away from $\bar{\Gamma}$–$\bar{K}$ is well resolved.

According to the calculations, the largest splitting occurs along the $\bar{P}$–$\bar{D}$ direction in the 3D BZ, as indicated in Fig. 4(a), which can be directly detected by varying the photon energies along the Γ–A direction. Red and blue colors correspond to opposite z components of spin in the M–Γ–A plane. Figure 4(b) shows the Fermi surface of the M–Γ–A plane. In the right half, there are four electron pockets, two on each side symmetrically distributed with opposite spins along the Γ–M direction. Two non-high-symmetry directions, $\bar{P}$–$\bar{D}$, indicated by the dashed lines, are spin non-degenerate. The two representative band dispersions along the D_1–P_1–D_1 ($k_y = 0.75\pi$) and D_2–P_2–D_2 ($k_y = 0.5\pi$) directions are presented in Figs. 4(c)–4(e) and Figs. 4(f)–4(h), respectively. The splitting bands near P_1 form four shallow electron pockets near the Fermi level, two on each side of P_1 with opposite spins, as shown in Fig. 4(e). The overall band structure is in good agreement with the DFT calculation without SOC, as shown in Fig. 4(c). Considering the effects of SOC on the band structure and spin splitting, as shown in Figs. 4(c) and 4(d), we compared the band structures with and without

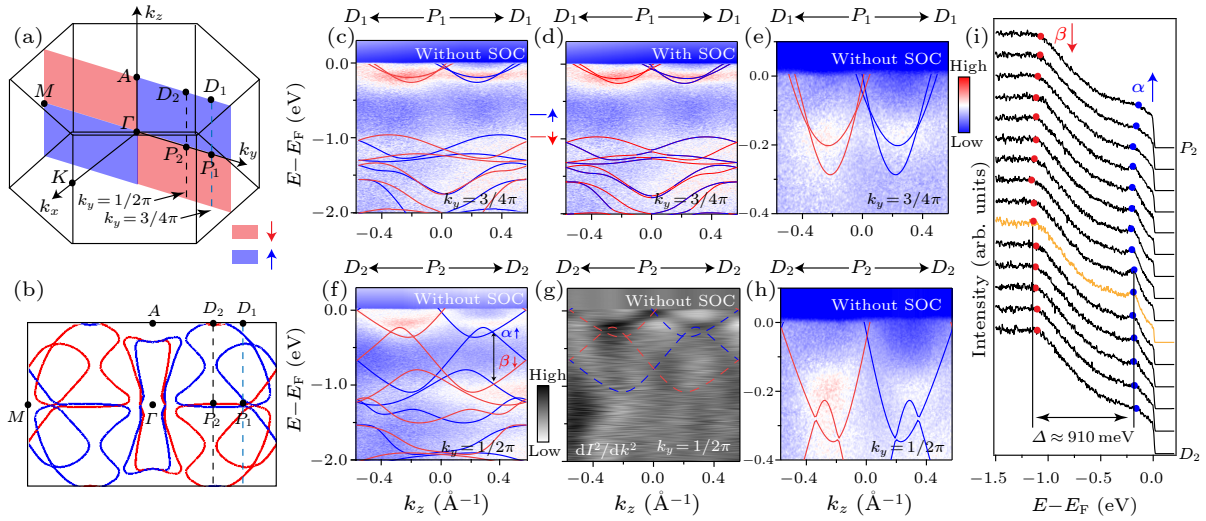

Fig. 4. Altermagnetic Splitting along the $\bar{P}$–$\bar{D}$ Direction. (a) Distribution of the $\bar{P}$–$\bar{D}$ direction at different k_y values in the 3D BZ. (b) Calculated Fermi surface of the M–Γ–A plane. (c) Photoemission intensity plot along the P_1–D_1 direction at $k_y = 3/4\pi$, appended with calculation without SOC. (d) Photoemission intensity plot along the P_1–D_1 direction at $k_y = 3/4\pi$, appended with calculation with SOC. (e) Zoomed-in spectra of (c). (f) Photoemission intensity plot along the P_2–D_2 direction at $k_y = 1/2\pi$, appended with calculation without SOC. The region indicated by the black arrow is the point of maximum splitting. (g) The second-derivative spectrum $\mathrm{d}I^2/\mathrm{d}k^2$ at $k_y = 1/2\pi$ appended with calculated dispersive bands. (h) Zoomed-in spectra of (f). (i) EDCs along the P_2–D_2 direction. The yellow curve highlights the spectra at $k_z = 0.35\,\text{Å}^{-1}$, showing the splitting energy ∼0.91 eV. The spectra of (c), (d), and (f) are normalized along the energy direction by a polynomial distribution extracted from $k_z = -0.45\,\text{Å}^{-1}$ and -0.55Å^{-1}, respectively, to enhance the visibility of the states near the Fermi level. All the data are taken at 7 K.

SOC at $k_y = 3/4\pi$. The influence of SOC on the splitting magnitude is very small and can be neglected. Moreover, both calculations yield agreement with the experimentally observed bands and band splittings. This confirms that the band structure we observed is robustly induced by altermagnetism and not dependent on the inclusion of SOC, which is consistent with the previous report.[35] At the $k_y = 0.5\pi$ along the D_2–P_2–D_2 direction, there are two spin-opposite electron pockets (α) near the Fermi level, along with flat bands at binding energies of 1 eV (β) and 2 eV, as shown in Fig. 4(f). To better reveal the band structure details, we performed second-derivative processing $\mathrm{d}I^2/\mathrm{d}k^2$ on the original spectra. As shown in Fig. 4(g), it highlights the dispersive bands corresponding to DFT results. Figure 4(i) shows the energy distribution curves (EDCs) indicating the positions of the α and β bands. By analyzing the energy splitting of the α and β bands at various momentum positions, we found that the largest energy splitting occurs at $k_z = 0.35\,\text{Å}^{-1}$, as indicated by the black arrow in Fig. 4(f), with a value of ∼910 meV, which is consistent with the band structure calculation and previous reports.[33,35] Interestingly, one could notice that the bands near the Fermi level consist of only two electron-like bands α along the P_2–D_2 direction, which are spin-antiparallel with respect to the P_2 point. This makes CrSb (100) thin film a great platform to explore the spin transport based on its altermagnetic properties.

In summary, we have successfully grown high-quality CrSb (100) thin films and investigated their altermagnetic electronic structures using high-resolution ARPES in combination with DFT calculations. Our results provide direct spectroscopic evidence for the 3D electronic structure and altermagnetic features of the CrSb thin film. The experimental data, particularly the observed altermagnetic splitting, are in good agreement with the DFT calculations, confirming the presence of spin splitting in the non-high-symmetry directions. Furthermore, our measurements reveal a large splitting of 910 meV along the P_2–D_2 direction, consistent with previous reports and theoretical predictions. It exhibits only altermagnetic band features near the Fermi surface along the $\bar{P}$–$\bar{D}$ direction, which minimizes interference from multiple energy bands. These characteristics make CrSb (100) thin films particularly suitable for future spintronic applications, offering a promising system for investigating and exploiting altermagnetism in thin-film architectures.

Methods. Epitaxial CrSb (100) thin films were grown on GaAs (110) substrates by MBE. Before growth, the GaAs (100) substrates were cleaned to remove the oxide layer through a sputtering and cleaning procedure using an argon sputter gun. The substrate temperature used for this procedure was 180 ℃ and the cleaning process was cycled three times to obtain a clean surface. Cr and Sb were used as the deposition sources with a flux ratio of 1:10, which was monitored by a quartz crystal microbalance. The substrate temperature during deposition was maintained at 230 ℃.

Synchrotron-ARPES measurements were carried out using synchrotron light sources at BL 03U of the Shanghai Synchrotron Radiation Facility (SSRF) in China. Lab-based ARPES experiments were carried out using a helium discharge lamp from Fermi Instrument. All the systems

are equipped with DA30 analyzers. The overall energy resolution was set to be better than 10 meV, and the angular resolution is ∼0.2°. The thin films were measured either *in situ* in the lab-based system or through a vacuum suitcase in the synchrotron-based system. All the measurements are at a base pressure better than 6×10^{-11} Torr, and during the transfer, the vacuum is kept better than 5×10^{-10} Torr.

DFT calculations were carried out using the Vienna *ab initio* simulation package (VASP).[41] The Perdew–Burke–Ernzerhof (PBE) exchange-correlation functional[42] was used within the projector augmented-wave method.[43,44] The lattice constants of CrSb were adopted as $a = b = 4.12$ Å and $c = 5.47$ Å. A plane-wave basis set with an energy cutoff of 500 eV was used, and the Brillouin zone integration was sampled using a Γ-centered Monkhorst-Pack k-point grid of $15 \times 15 \times 11$.[45] The electronic iterations were performed until the total energy change between successive steps fell below 10^{-7} eV, ensuring high numerical precision. The standard PBE potentials were used for the pseudopotentials, with six valence electrons ($3d_5$, $4s_1$) for Cr and five valence electrons ($5s_2$, $5p_3$) for Sb. Spin-polarized calculations were carried out to account for magnetic interactions. The calculated band structures were further adjusted to align with experimental ARPES data by applying a renormalization factor of 1.37 and shifting the Fermi energy E_F upward by 300 meV.

Acknowledgements. This work was supported by the National Key R&D Program of China [Grant No. 2023YFA1406304 (J J)], the National Natural Science Foundation of China [Grant No. 12174362 (J J)], the Innovation Program for Quantum Science and Technology [Grant No. 2021ZD0302803 (D L F)], and the New Cornerstone Science Foundation (D L F). Part of this research used Beamline 03U of the Shanghai Synchrotron Radiation Facility, which is supported by ME2 project under contract No. 11227902 from the National Natural Science Foundation of China.

References

[1] Šmejkal L, Sinova J, and Jungwirth Tomas 2022 *Phys. Rev. X* **12** 031042
[2] Šmejkal L, Sinova J, and Jungwirth Tomas 2022 *Phys. Rev. X* **12** 040501
[3] Liu Q H, Dai X, and Blügel S 2025 *Nat. Phys.* **21** 329
[4] Chappert C, Fert A, and Dau F N V 2007 *Nat. Mater.* **6** 813
[5] Ralph D C and Stiles M D 2008 *J. Magn. Magn Mater.* **320** 1190
[6] Bhatti S, Sbiaa R, Hirohata A, Ohno H, Fukami S, and Piramanayagam S N 2017 *Mater. Today* **20** 530
[7] Bader S D and Parkin S S P 2010 *Annu. Rev. Condens. Matter Phys.* **1** 71
[8] Ma H Y, Hu M L, Li N N, Liu J P, Yao W, Jia J F, and Liu J W 2021 *Nat. Commun.* **12** 2846
[9] Wu C J, Sun K, Fradkin E, and Zhang S C 2007 *Phys. Rev. B* **75** 115103
[10] Naka M, Hayami S, Kusunose H, Yanagi Y, Motome Y, and Seo H 2019 *Nat. Commun.* **10** 4305
[11] Gonzalez-Hernandez R, Šmejkal L, Vyborny K, Yahagi Y, Sinova J, Jungwirth T, and Železný J 2021 *Phys. Rev. Lett.* **126** 127701
[12] Bose A, Schreiber N J, Jain R, Shao D F, Nair H P, Sun J X, Zhang X S, Muller D A, Tsymbal E Y, Schlom D G, and Ralph D C 2022 *Nat. Electron.* **5** 263
[13] Bai H, Han L, Feng X Y, and Zhou Y J 2022 *Phys. Rev. Lett.* **128** 197202
[14] Karube S, Tanaka T, Sugawara D, Kadoguchi N, Kohda M, and Nitta J 2022 *Phys. Rev. Lett.* **129** 137201
[15] Šmejkal L, González-Hernández R, Jungwirth T, and Sinova J 2020 *Sci. Adv.* **6** eaaz8809
[16] Feng Z X, Zhou X R, Šmejkal L *et al.* 2022 *Nat. Electron.* **5** 735
[17] Reichlova H, Seeger R L, González-Hernández R *et al.* 2020 arXiv:2012.15651 [cond-mat.mes-hall]
[18] Mazin I I, Koepernik K, Johannes M D, and González-Hernández R 2021 *Proc. Natl Acad. Sci.* **118** e2108924118
[19] Samanta K, Ležaić M, Merte M, and Freimuth F 2020 *J. Appl. Phys.* **127** 213904
[20] Naka M, Hayami S, Kusunose H, Yanagi Y, Motome Y, and Seo H 2020 *Phys. Rev. B* **102** 075112
[21] Naka M, Motome Y, and Seo H 2022 arXiv:2208.11823 [cond-mat.str-el]
[22] Hellenes A B, Jungwirth T, Sinova J, and Šmejkal L 2024 arXiv:2309.01607 [cond-mat.mes-hall]
[23] Lee S Y, Lee S, Jung S *et al.* 2024 *Phys. Rev. Lett.* **132** 036702
[24] Krempasky J, Šmejkal L, D'Souza S W *et al.* 2024 *Nature* **626** 517
[25] Liu Z Y, Ozeki M, Asai S, Itoh S, and Masuda T 2024 *Phys. Rev. Lett.* **133** 156702
[26] Hajlaoui M, D'Souza S W, Šmejkal L *et al.* 2024 *Adv. Mater.* **36** 2314076
[27] Osumi T, Souma S, Aoyama T, Yamauchi K, Honma A, Nakayama K, Takahashi T, Ohgushi K, and Sato T 2024 *Phys. Rev. B* **109** 115102
[28] Zhang F, Cheng X, Yin Z *et al.* 2024 arXiv:2407.19555 [cond-mat.str-el]
[29] Jiang B, Hu M Z, Bai J L *et al.* 2024 arXiv:2408.00320 [cond-mat.mtrl-sci]
[30] Liu J Y, Zhan J, Li T R *et al.* 2024 *Phys. Rev. Lett.* **133** 176401
[31] Zhou Z Y, Cheng X K, Hu M L, Chu R Y, Bai H, Han L, Liu J W, Pan F, and Song C 2025 *Nature* **638** 645
[32] Reimers S, Odenbreit L, Šmejkal L *et al.* 2024 *Nat. Commun.* **15** 2116
[33] Ding J Y, Jiang Z, Chen X *et al.* 2024 *Phys. Rev. Lett.* **133** 206401
[34] Zeng M, Zhu M Y, Zhu Y P *et al.* 2024 *Adv. Sci.* **11** 2406529
[35] Yang G, Li Z, Yang S *et al.* 2025 *Nat. Commun.* **16** 1442
[36] Lu W L, Feng S Y, Wang Y, Chen D, Lin Z H, Liang X, Liu S Y, Feng W X, Yamagami K, Liu J W, Felser C, Wu Q S, and Ma J Z 2024 arXiv:2407.13497 [cond-mat.mtrl-sci]
[37] Li C, Hu M, Li Z *et al.* 2024 arXiv:2405.14777 [cond-mat.mtrl-sci]
[38] Chandrasekhar S 1960 *Adv. Phys.* **9** 363
[39] Sabine T M 1988 *Acta Cryst.* **44** 368
[40] Markiewicz R S, Sahrakorpi S, Lindroos M, Lin H, and Bansil A 2005 *Phys. Rev. B* **72** 054519
[41] Kresse G and Furthmuller J 1996 *Phys. Rev. B* **54** 11169
[42] Perdew J P, Burke K, and Ernzerhof M 1996 *Phys. Rev. Lett.* **77** 3865
[43] Kresse G and Joubert D 1999 *Phys. Rev. B* **59** 1758
[44] Blöchl P E 1994 *Phys. Rev. B* **50** 17953
[45] Monkhorst P E and Pack J D 1976 *Phys. Rev. B* **13** 5188